THE JOURNAL OF PHYSICAL CHEMISTRY C

Article

pubs.acs.org/JPCC

The Mobility of Water Molecules through Hydrated Pores

Natalia Pérez-Hernández,[†,⊥] Trung Quan Luong,[‡] Martín Febles,[§] Carlos Marco,[∥] Hans-Heinrich Limbach,[⊥] Martina Havenith,[‡] Cirilo Pérez,[§] María Victoria Roux,[#] Ricardo Pérez,[†] and Julio D. Martín*[,†]

[†]Instituto de Investigaciones Químicas, CSIC, Avenida Américo Vespucio 49, 41092 Seville, Spain

[‡]Lehrstuhl für Physikalische Chemie 2, Ruhr-Universtät Bochum, 44780 Bochum, Germany

[§]Instituto de Bioorgánica, Universidad de La Laguna- CSIC, Carretera Vieja de La Esperanza 2, 38206 La Laguna, Tenerife, Spain

[∥]Instituto de Ciencia y Tecnología de Polímeros, CSIC, Juan de la Cierva 3, 28006 Madrid, Spain

[⊥]Institut für Chemie und Biochemie, Freie Universität Berlin, Takusstrasse 3, D-14195 Berlin, Germany

[#]Instituto de Química Física Rocasolano, CSIC, Serrano 119, 28006 Madrid, Spain

Supporting Information

ABSTRACT: To achieve a more exact understanding of the water transport in natural channels, a series of non-natural structures have been developed. They have been studied by far-infrared spectroscopy, solid-state nuclear magnetic resonance, differential scanning calorimetry, thermogravimetric analysis, and variable-temperature powder X-ray diffraction to examine the behavior of water at the molecular level. Water in these predominantly nonpolar pores can be metastable, with filling and emptying occurring upon changes in solvent conditions. The water contained in these pores exhibits a dynamics that might be controlled, since it depends on the structural features of the monomers that form the pore "skeleton". We have observed changes in the pore diameter depending on the selected isomer. This provokes at a given temperature differences in the arrangement and dynamics of the contained water. The water dynamics increases with both temperature and pore diameter in a process that is reversible over a temperature range specific for each structure. Beyond this particular temperature threshold, the pore water can be irreversibly evacuated, and at this point a decrease of the dynamics is observed. The slower dynamics of the remaining water in partially evacuated pores is probably due to the increased interaction with the inner-pore surface owing to a concomitant narrowing of the pore. These findings not only highlight the need for the presence of freely moving water inside the pore to sustain its permeability by water, but also point to the decrease in the dynamics of the remaining water in partially evacuated pores.

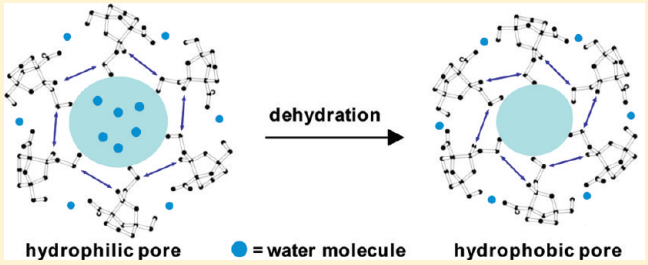

INTRODUCTION

Permeation of water across cellular membranes is facilitated by aquaporins,[1,2] a family of proteins that associate as tetramers to form cylindrical transmembrane pores 20−30 Å long and about 3 Å wide at their narrowest point. However, a detailed understanding of the forces that drive the filling of the pores by water and the functional thermodynamics of these predominantly hydrophobic natural pores remains elusive, despite recent progress.[2,3] A full understanding of the transport of water requires knowledge at the molecular level of the equilibrium and peculiar behaviors of the short-lived local structures of the entrapped water.[4−7]

The structure of water in natural channels has been studied using molecular dynamics simulations,[8] but these biological systems are characterized by numerous chemical and structural complexities. Simpler artificial models will permit more straightforward evaluations.[8−10] Single-walled carbon nanotubes (SWCNTs) are one of the simplest model systems specifically valid for modeling the diffusion of water in biological structures and have been used with the aquaporin water channel[11−15] as well as other nanofluid systems.[16−19] The most realistic computational strategies modeled the structural and dynamic properties of water in SWCNT and revealed concerted water motions and density distribution patterns.[8−15] However, the application of these nanoporous media to the study of the structure and dynamics of long-lived aggregates of water molecules is limited by the inability to sustain the mechanisms determined *in silico* in discrete experiments.[20−25] Molecular dynamics simulation studies conducted at room temperature predicted that the structure and dynamics of water are specific to each model and depend on the inner diameter[26−29] and hydrophilicity[30,31] of the pore. Yet, experimental evidence supporting this conclusion is lacking,

Received: February 9, 2012
Revised: April 11, 2012
Published: April 12, 2012

Chart 1. Synthesized Monomers with Linear Appendages[a]

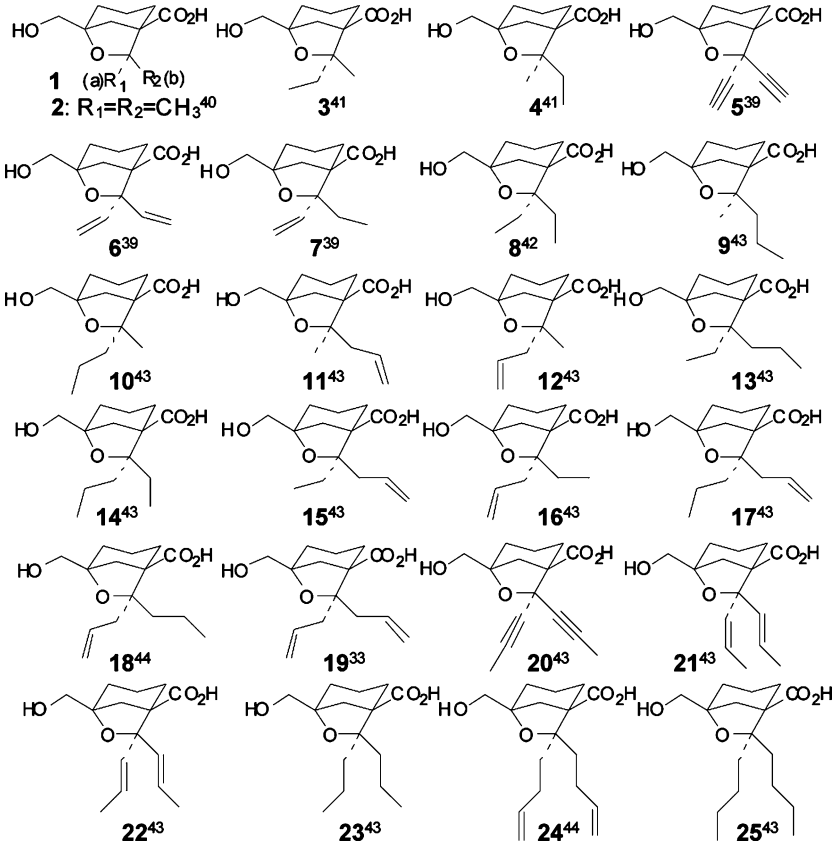

[a]The upper numbers show related references.

and rigorous understanding of the mechanisms of water transport and conduction through pores remains incomplete.[32]

In natural water channels,[2] factors such as diameter and hydrophobicity/hydrophilicity are nonuniform along the pore; therefore the structure and dynamics of water molecules should change according to their momentary location. Water diffusion would then be the result of balances among the transient local structures and dynamics of water molecules present within the pore. The lack of hydrogen-bonding interactions between the water and the inner surface of the pore has prevented even preliminary experiments that address questions concerning the structural nature of water that can occupy a nonpolar pore, even though a range of distinct studies concerning the occupation of water have been carried out by computer simulations.[8−10]

We have previously studied the dynamics of the water contained in pores as a function of the temperature and of the inner pore diameter, and have reported our observations in the context of thermodynamic processes that determine the crystal structure and the water diffusion mechanism in the pores.[33] To extend these studies, we synthesized solid-state porous organic assemblies as chemical models that were composed of several homologous molecules that varied in the length and nature of the flexible appendages. These synthetic structures with variations in the width of the pores allowed us to investigate the mechanisms of biological water transport. In this work, our specific objective is to address and explain the relationship between water dynamics and the dynamics of the immediate organic structural components that define the pore's interior. In a broader context, these findings will contribute to a better comprehension of water dynamics in nonpolar environments.

RESULTS AND DISCUSSION

Models of Water Channels. Synthetic chemical methods have not been well integrated into the study of the chemical processes mediated by water in biological systems.[34,35] We have attempted to explain the formation of biological channels in terms of a unique thermodynamic process where the supramolecular structure is stoichiometrically sustained by the organic monomers and water molecules according to the general eq 1.[36] It describes the synthesis of long-lived water clusters from bulk water, where n represents the number of organic monomers, and m is the number of water molecules involved in the resulting assembly.

$$\underset{\text{(Monomers)}}{n\text{M}} + \underset{\text{(Bulk water)}}{m\text{H}_2\text{O}} \rightleftarrows \underset{\text{(Hydrated pore)}}{\text{M}_n\cdot(\text{H}_2\text{O})_m} = \underset{\text{(Anhydrous pore)}}{\text{M}_n} + \underset{\text{(Water cluster)}}{(\text{H}_2\text{O})_m} \quad (1)$$

Following a process in which explanatory hypotheses are initially formulated and subsequently evaluated,[37,38] we designed solid-state porous organic assemblies as chemical models and used them to elucidate the mechanisms of biological water transport.[36] We synthesized a wide range of homologues of the general structure (±)**1**·nH$_2$O (Charts 1 and 2) by changing the number and nature of selected atoms in

dx.doi.org/10.1021/jp301323c | J. Phys. Chem. C 2012, 116, 9616−9630

Chart 2. Synthesized Monomers with Branched, Cyclic, and Oxygenated Appendages[a]

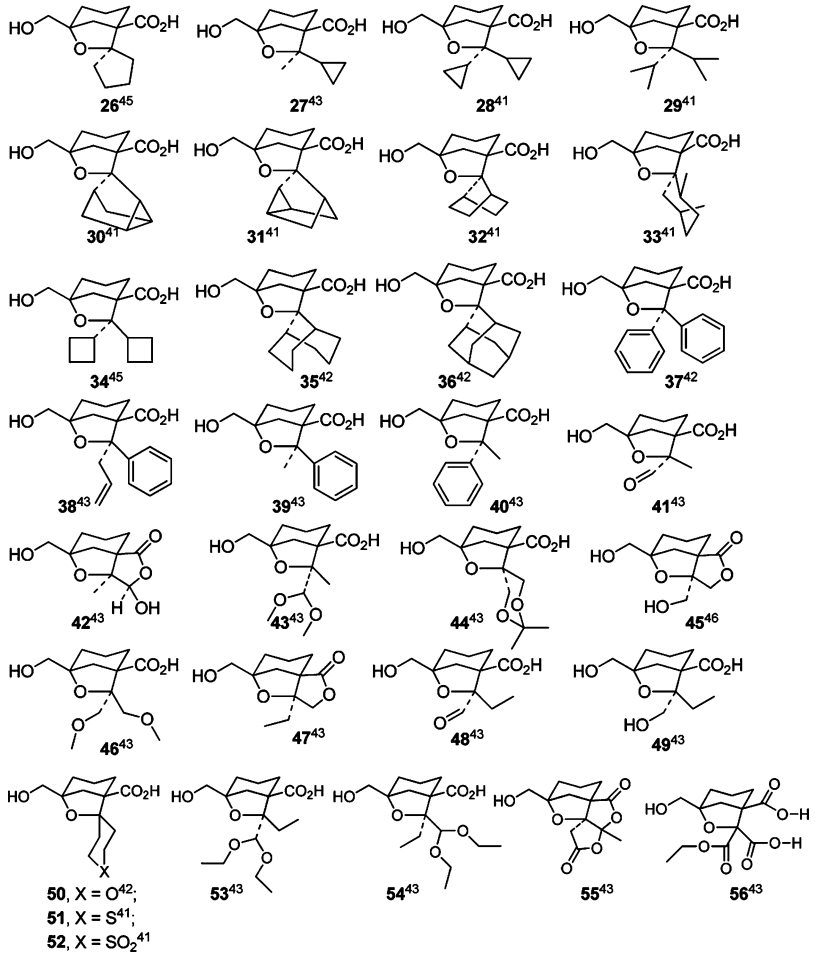

[a]The upper numbers show related references.

appendages, and studied their structural influence in the solid state crystalline structures following a previously published synthetic methodology developed in our group.[39] Several of these compounds appeared to be promising candidates to give hollow tubular structures, while other molecules were chosen to probe the structural requirements. Crystals from all compounds were slowly grown under identical conditions using a previously water-saturated mixture of carbon tetrachloride/2,2,4-trimethylpentane mixture (4:1). From the more than 50 homologues prepared, only 12 molecules (**8**–**19**), with flexible linear appendages (Chart 1), gave hydrated crystalline structures by incorporation of a maximum of two water molecules for each organic monomer, (±)**8**·2H_2O–(±)**19**·2H_2O, forming pseudoisomorphic porous structures with identical three-dimensional hydrogen-bonded networks (Figure 1). Identical crystallization behavior was observed for hydrated crystals of any of the compounds formed by molecules **8**–**19**. Indeed, the slow growing crystals of general structure (±)**1**·*n*H_2O gave highly transparent macrotubes and partially hollow semitubes that could be observed with the naked eye.[36] Anhydrous structures of the general structure (±)**1** formed solid prisms.

Of the homologues with branched and cyclic appendages that restricted conformational movement (Chart 2), only two were derived from interdigitated single-stranded head-to-tail chains incorporated water molecules: (±)**31**·H_2O and (±)**36**·1/2H_2O.[42] The rest of the compounds, including the homologues with oxygenated appendages, generated an anhydrous packing composed mostly of double-stranded head-to-tail arrays. These results proved that when structurally robust hydrogen-bonding patterns are employed, the combined steric requirements and the conformational flexibility of the appendages govern which framework is adopted. Thus, we argue that the desired architecture of the target material can be achieved by systematic changes in the size of monomers.

This work particularly features the structure and dynamics of water confined inside the pores formed by molecules **8** and **19** by means of monocrystal X-ray diffraction (XRD),[33,41] variable-temperature powder X-ray diffraction (VT-PXRD) experiments,[47] differential scanning calorimetry (DSC),[33,47] thermogravimetric analysis (TGA),[33,47] attenuated total reflection infrared (ATR-IR),[48] far-infrared (FIR)[44] spectroscopy, and solid state nuclear magnetic resonance (SSNMR).[33] Two apparently different types of water molecules were observed: (i) water molecules located at the surface that remained mainly in the H-bonding pattern from which the porous structure is built up, and (ii) water molecules in delocalized clusters stabilized by hydrogen bonding within the cluster and by van der Waals interactions with the nonpolar carbon-appendages distributed along the inner surface of the pore (Figure 1). However, hydrogen bonds per se do not immobilize a water molecule, as seen by considering bulk water, and in the structures, both types of water molecules exist in equilibrium. Water in these

dx.doi.org/10.1021/jp301323c | J. Phys. Chem. C 2012, 116, 9616–9630

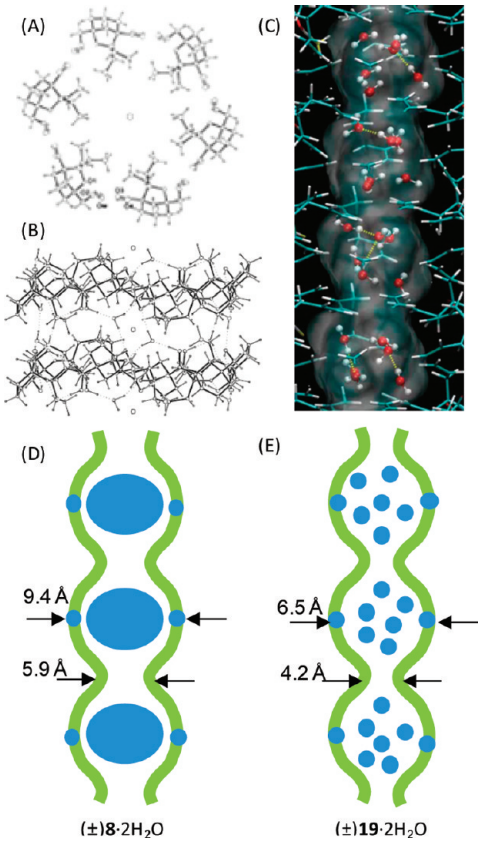

Figure 1. (A–C) Crystal structures of (±)**8**·2H_2O[41] and (±)**19**·2H_2O.[33] (A) Hexameric association of (±)**8**·2H_2O, viewing down from the top. (B) Side view of two stacked hexameric units of (±)**8**·2H_2O; the water molecules involved in fixing of the tubular structure are linked with dotted lines. (C) Side view of the crystal structure of (±)**19**·2H_2O in a capped-stick representation. Disordered water oxygen and hydrogen atoms are shown in red and white, respectively. (D,E) Schematic pore profile of pores (±)**8**·2H_2O and (±)**19**·2H_2O where typical average diameter sizes are indicated. The water inside the pore in (±)**8**·2H_2O is diffuse (fat blue ellipse) and less structured than in (±)**19**·2H_2O, where it is represented by individual circles.

predominantly nonpolar cavities can be metastable, with filling and emptying of the pores occurring upon changes in solvent conditions. Thus, when deuterated water is used to label the samples in the gas phase, deuterium is slowly and reversibly incorporated in all mobile protons of the pore structure.[33,48]

If water in cavities is disordered, it is hard to detect with diffraction methods.[49−52] However, in the pore with structure (±)**19**·2H_2O, X-ray crystallographic data[33] accounted not only for the location of the water molecules H-bonded to the pore surface, but also for clusters formed by water inside the pore due to the reduced diffusion rate because of the narrower diameter as compared to (±)**8**·2H_2O (Figure 1C). Our previous results[44] showed that the FIR frequency region from 400 to 570 cm^{-1} is a sensitive tool to probe the translational mobility of water molecules inside hydrated pores. Furthermore, the temperature dependence of the FIR absorbance of water in hydrated pores differs markedly depending on the inherent water dynamics in each structure imposed by the inner diameter of the pore. Less confined and thus more mobile water molecules inside larger pores show a large change in their absorbance upon increase of temperature, similar to that observed in bulk liquid water. On the other hand, water molecules confined in narrow pores owing to their higher interaction with the pore wall showed a smaller increase in a sorbance when the temperature was varied between −5 and 20 °C.[44]

In Figure 2, some of these features are shown over the crystal structures formed by (±)**8**·2H_2O and (±)**19**·2H_2O; the nonpolar contacts between the appendages as well as the definition of the diameter by the substituents in β have been depicted. The terminal methylene carbon in β in compound (±)**19**·2H_2O is the cause of the narrower diameter of the pore formed by this compound. Single-crystals of the new compounds (±)**9**·2H_2O–(±)**18**·2H_2O were studied by single X-ray crystallography, but structural details were not made available in advance of the structure solution studies described herein.

The appendages R_1 and R_2 in the molecules **9**–**18** were chosen to cover different lengths and polarities and their effect in crystalline structure hydration could be independently studied (Chart 1). It is expected that in the diastereomeric pairs formed by **9**–**10**, **11**–**12**, **13**–**14**, **15**–**16**, and **17**–**18**, isomers **9**, **11**, **13**, **15**, **17**, and **18** exhibit hydrated pores of similar diameters. These are expected to show a similar behavior of their water dynamics, which should also be comparable to that observed in the pore formed by (±)

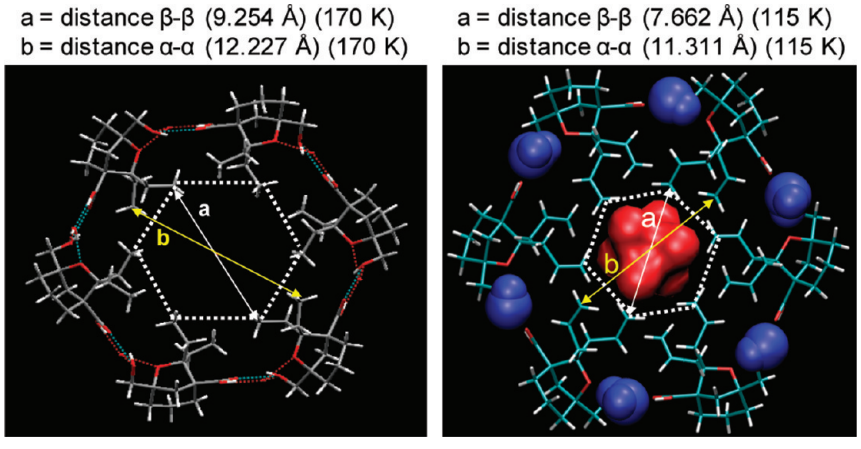

Figure 2. Crystal structure of (±)**8**·2H_2O[41] (left) and (±)**19**·2H_2O[33] (right). The white dotted lines show the β-oriented appendages that define the internal pore diameter. The distances *a* and *b* correspond to the maximum distance between the β and α oriented appendages, respectively.

dx.doi.org/10.1021/jp301323c | J. Phys. Chem. C 2012, 116, 9616–9630

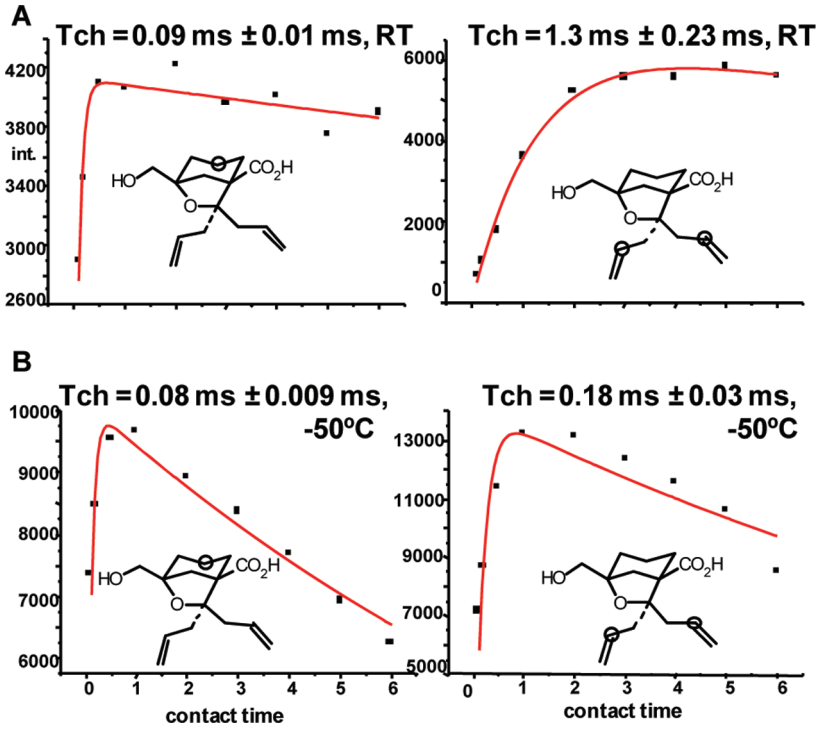

Figure 3. $^{1}H \rightarrow {}^{13}C$ CP magnetization transfer build up curves and T_{CH} values for nuclei in a core carbon and in the appendage (indicated by circles) at room temperature (A) and −50 °C (B).

19·2H_2O, of similar diameter. On the other hand, isomers **10**, **12**, **14**, and **16** will give rise to different pore sizes depending on the β oriented appendage. Structures **14** and **16** should exhibit water dynamics close to the values observed for (±)**8**·2H_2O. We also anticipated that molecules **10** and **12** with β oriented methyl substituents would most likely give rise to anhydrous structures, as is the case in their molecular homologues **2** and **3**.

SSNMR Analysis of Reference Tubular Structure (±)19·2H_2O. In the tubular structures (±)**8**·2H_2O and (±)**19**·2H_2O, the enthalpic change observed at the lowest temperature occurred over the same temperature interval at which a drastic change in the pore water mobility was observed by ^{2}H SSNMR.[33] To study the influence of the carbon appendages, we performed H → ^{13}C cross-polarization (CP) magic angle spinning (MAS) NMR experiments on (±)**19**·2H_2O and obtained values of T_{CH} by performing variable contact time experiments as well as ^{13}C T_1 times at different temperatures for ^{13}C appendages nuclei.[53−55] Since the dipolar coupling is strongly affected by motion, a small or large value of T_{CH} indicates rigidity or flexibility, respectively.[53] A comparison of the build-up curves and T_{CH} values for carbons in the core and in the appendages of the molecule at two different temperatures (Figure 3) showed that, at room temperature, T_{CH} is ∼14-fold larger for the "appendage carbon" (Figure 3A), indicating a much higher mobility in this position. Decreasing the temperature to −50 °C decreased the T_{CH} value to ∼14% of the value at room temperature, while it remained almost unaltered for the carbon in the ring (Figure 3B). Thus, the mobility of the appendages is affected by temperature to a greater extent than the carbon in the ring.

We also performed ^{13}C longitudinal relaxation time T_1 measurements of representative carbons in the temperature interval of interest (Supporting Information (SI), Figure 1A). We previously established the T_1 dependence on temperature in the observed temperature interval for each of the studied nuclei. The solid state carbon nuclei correlation times are assumed to be long. In such cases, large T_1 values suggest long correlation times, i.e., less mobility, and vice versa.[56−58] Again, two representative carbons were analyzed, one in the core of the molecule and one in the more flexible propenyl chain. The results agreed with previous observations, as, for the appendage carbons, the value of T_1 fell by 3-fold, indicating more mobility in the carbons of the allyl chain that are oriented toward the center of the pore and are thus in closer contact to the pore water. Interestingly, in a sample of (±)**19**·2H_2O exposed to D_2O vapor (thus exhibiting deuterated exchangeable proton sites), the only carbon exhibiting a reduced T_1 was the CH_2 influenced by the exchange of the alcoholic OH by OD. As the decrease is not observed for the terminal carbons close to pore water, an intermolecular contribution to the relaxation cannot be invoked (SI, Figure 1B).[59] Moreover, these results point to an additional contribution from the alkyl appendages to enthalpic changes previously observed and initially assigned to water channels.[33]

Reversibility of the Pore Water Dynamics in Structures (±)8·2H_2O and (±)19·2H_2O Studied by FIR Spectroscopy. The structures formed by (±)**8**·2H_2O and (±)**19**·2H_2O can be considered to represent "wide pore" and "narrow pore" models, respectively. We applied the useful correlation between water dynamics and the FIR absorbance of the samples to study the reversible nature of this correlation with respect to the dependence on temperature. We extended the previous temperature-dependent experiments and performed a series of measurements in which the samples were first heated and then cooled (Figure 4).

Over the temperature interval −5 °C ↔ 30 °C, the changes in absorbance were completely reversible for the hydrated wide pore formed by (±)**8**·2H_2O. This reversibility is expected as the amount of water remains unchanged upon tuning the temperature. Indeed, the loss of some of the pore water started

dx.doi.org/10.1021/jp301323c | J. Phys. Chem. C 2012, 116, 9616−9630

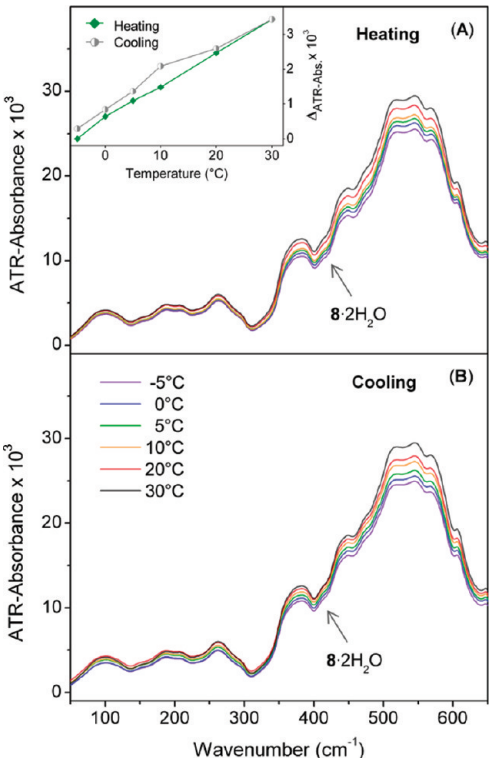

Figure 4. Reversible changes in the absorbance of the hydrated pore (±)**8**·2H_2O upon heating (A) and cooling (B) the sample in the temperature interval −5 °C ↔ 30 °C. The color code is the same for both situations, and it is represented in B. Inset: Plot representing reversible behavior the integrated absorbance over the frequency range from 400 to 570 cm^{-1} upon heating and cooling the sample.

only when the temperature reached 40 °C, without the collapse of the pore structure.[47] The decrease in absorbance was observed in the FIR spectra obtained after heating the sample at 40 °C for 30, 60, and 90 min (Figure 5). After 60 min, the

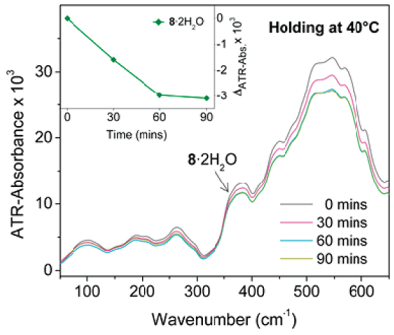

Figure 5. Monitoring of the mobile water content of the pores of (±)**8**·2H_2O at 40 °C by FIR spectroscopy. Inset: Plot representing the difference in the integrated absorbance over the frequency range from 400 to 570 cm^{-1} versus time.

entire content of mobile water had been lost, and no additional decrease in absorbance was observed in the absorbance after a total of 90 min heating. This outcome agreed with previous results.[47]

As previously observed,[47] water is not reincorporated, even after keeping the sample under moist conditions for 24 h. The release of the mobile fraction of water rendered the pore more hydrophobic. Thus the FIR absorbance is independent of temperature, as illustrated in Figure 6. The fully hydrated as-synthesized structure (±)**8**·2H_2O showed the highest increase

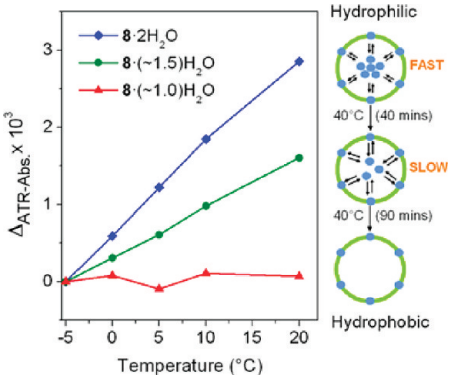

Figure 6. Graph showing the change in the integrated absorbance of differently hydrated (±)**8**·nH_2O compared with absorbance at −5 °C over the frequency range from 400 to 570 cm^{-1}, obtained by cooling of the sample after exposing for variable periods to 40 °C (left panel). Scheme illustrating the change of the hydration in the pore upon heating. Pore walls are depicted in green, and the water molecules are depicted as blue circles (right panel).

in absorbance with increasing temperature. For the partially dehydrated sample, (±)**8**·(~1.5)H_2O, obtained by holding the sample at 40 °C for 40 min prior to cooling, the slope of the curve defining changes in absorbance as a function of temperature is approximately half that of the fully hydrated sample. When the freely moving water is fully evacuated by heating the sample for 90 min at 40 °C, we obtained the structure (±)**8**·(~1.0)H_2O. The absorbance in this case was independent of temperature.

Repeating these studies on the narrow pore model structure (±)**19**·2H_2O showed a similar trend (S I, Figure 3). Notably, the release of water began at lower temperatures. This was suggested by previous TG experiments[47] and was observed in the present work for the pores formed by molecules (±)**9**, (±)**17**, and (±)**18**, which readily lost water at room temperature.

Study of the Structures Formed by (±)1, $R_1 \neq R_2$. We also studied the purified structures achieved from the pairs of diastereomers of the general formula of (±)**1** with different appendages ($R_1 \neq R_2$): **9**−**10** (methyl/propyl), **11**−**12** (methyl/allyl), **13**−**14** (ethyl/propyl), **15**−**16** (ethyl/allyl), and **17**−**18** (propyl/allyl) (Chart 1). These molecules are differently substituted with one, two, or three/three carbon appendages affording hydrated tubular structures, with the only exceptions being compound **10**, which gave nonporous anhydrous structures, and compounds **16** and **17**, which afforded both anhydrous (nonporous) and hydrated (porous) crystals. The crystal packing of **15** could not be determined due to difficulties in obtaining suitable single crystals uncontaminated with the diastereomer **16**.

Anhydrous Nonporous Packings of General Structure (±) ***1***. First, we performed a comparative investigation of anhydrous structures including the three above-mentioned structures (±)**10**, (±)**16**, and (±)**17**, as well as other structures of the newly synthesized molecules (Charts 1 and 2) possessing identical ($R_1 = R_2$) or different ($R_1 \neq R_2$) appendages, that gave anhydrous structures under any crystallization circumstances. The molecules with identical appendages were (±)**6**, (±)**23**, (±)**29**, and (±)**37**. The molecules with different appendages were (±)**38**, (±)**39**, (±)**40**, and (±)**49**.

dx.doi.org/10.1021/jp301323c | J. Phys. Chem. C 2012, 116, 9616−9630

The low-temperature DSC experiments from 150 to 283 K showed enthalpy changes associated with variations in the conformational mobility of the appendages in each monomer. Approximately the same pattern of enthalpy variations upon changes in temperature was observed for anhydrous structures (see further). DSC and TG data for all compounds can be found in the SI. Since the bicyclic core is conformationally rigid, and the mobility of the carboxylic acid and of the hydroxymethyl substituents is restricted due to involvement in the hydrogen bond network that sustains the structure, we expected that the observed reversible enthalpy changes with temperature were caused by the freely moving appendages at the oxolane ring. In studies in which previously cooled samples were reheated, the compounds in which $R_1 = R_2$ exhibited enthalpy modifications characterized by two broad endotherms. Temperature intervals and enthalpy variations were very similar and dependent on their previous cooling rate. The temperature intervals of the enthalpy modifications at lower temperature were larger, while the temperature ranges of the second modification intervals at higher temperature became shorter (Table 1). This was associated with a high degree of organization of the molecular appendages.

Table 1. Observed Endotherms by DSC[a] of Selected Anhydrous Structures of General Formula (±)1 ($R_1 = R_2$)

compound	interval (K)	$\Delta H°$ (J/g)	interval (K)	$\Delta H°$ (J/g)
(±)**6**	204.6 → 230.2	0.6	240.4 → 265.2; 265.2 → 280.2	1.0
(±)**23**	187.1 → 199.6; 204.8 → 221.0; 227.6 → 234.7	0.4	252.5 → 270.2	0.3
(±)**29**	209.7 → 247.2	1.0	247.2 → 260.4	0.1
(±)**37**	184.7 → 241.0	1.3	241.0 → 255.2	0.1

[a]Temperature intervals and changes in enthalpy found when heating (rate of 10 K/min) previously cooled samples (cooling rate of 5 K/min).

For compounds in which $R_1 \neq R_2$, the behavior is more complex, and several modifications were observed, which was indicative of higher molecular disorder. In all the structures studied, the previous cooling rate strongly influenced the result observed in the heating (SI, Table 1).

We also studied the temperature dependence in the FIR absorption spectra of structures (±)**10**, (±)**16**, and (±)**17** as well as for selected anhydrous nonpore structures (Figure 7). The FIR spectra show an almost constant absorbance at different temperatures, which is indicative of the absence of water.[44]

*Hydrated Pores of General Structure (±)**1**·n(H_2O).* *(i). Hydrated Porous Structures Including One/Three Carbon Appendages.* Structures possessing methyl/propyl, (±)**9**·nH_2O, and methyl/allyl, (±)**11**/**12**·2H_2O, appendages were also studied. While the structure generated by crystallization of isomer **10**, which possesses β-methyl/α-propyl appendages, is anhydrous, its diastereomer **9** with the methyl group oriented in the α configuration always gave rise to hydrated porous structures. The content of water in structures (±)**9**·nH_2O varied since a certain amount of water is lost at room temperature after the crystallization. The loss of water was reflected in the TGA, DSC, and FIR studies, depending on how much time passed before the corresponding measurements were performed. The TGA results for the anhydrous sample (±)**10** were compared with four samples of (±)**9**·nH_2O with a similar dehydration profile but with different content of water, (±)**9**·(0.96)H_2O, (±)**9**·(1.01)H_2O, (±)**9**·(1.40)H_2O, (±)**9***·(1.37)H_2O (Figure 8). The (±)**9***·(1.37)H_2O sample exhibited the highest degree of purity for isomer **9**, whereas the other three samples are contaminated by its diastereomer **10** (<10%).

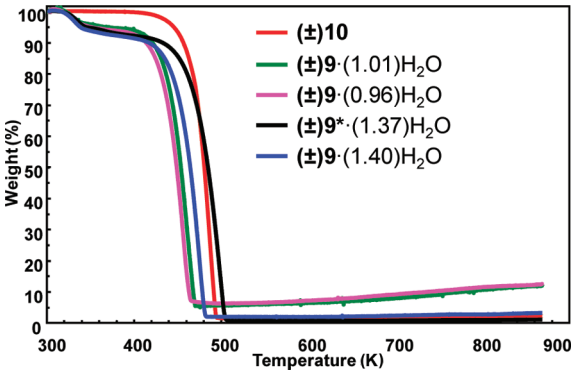

Figure 8. TGA results for the anhydrous structure (±)**10** and (±)**9**·nH_2O.

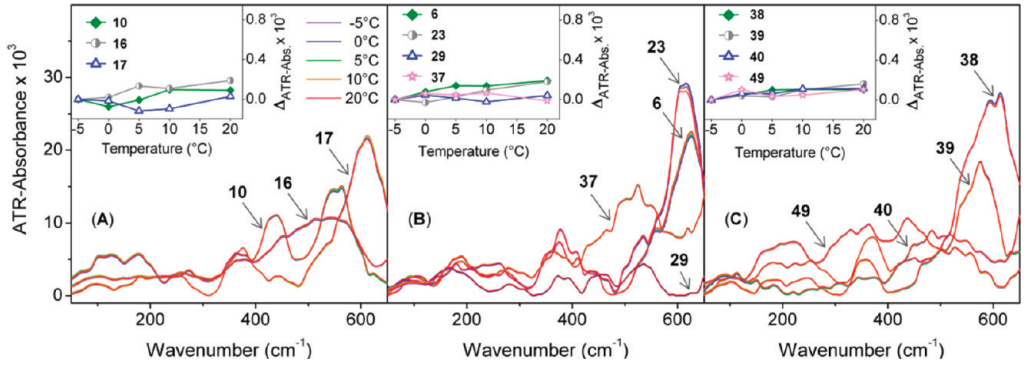

Figure 7. The effect of temperature on the FIR absorbance of anhydrous structures. The FIR absorbance values over the range from 400 to 570 cm^{-1} were obtained for the indicated anhydrous structures. (A) Anhydrous packings of racemic molecules: **10**, **16**, and **17**. (B,C) Anhydrous nonporous structures of additional molecules with identical (B) and different (C) appendages. Insets: Plots of the difference in integrated absorbance over the frequency range from 400 to 570 cm^{-1} at different temperatures.

dx.doi.org/10.1021/jp301323c | J. Phys. Chem. C 2012, 116, 9616−9630

Table 2. Observed Endotherms by DSC[a] of Hydrated Structures (±)9·*n*H2O and (±)11/12·2H_2O

compound	interval (K)	interval (K)	interval (K)	interval (K)	interval (K)	interval (K)	interval (K)	$\Delta H°$ (J/g)
(±)**9** (1.01)H_2O	151.6 →164.8	166.1 → 184.5	188.2 → 210.2	210.3 →226.1	227.3 →241.3	241.5 →254.9	257.7 →277.2	10.1
(±)**9** (1.40)H_2O		176.9 →188.6	188.6 → 202.6	202.6 → 221.3	220.6 →249.3	254.4 →268.8	272.4 →287.7	2.66
(±)**9*** (1.37)H_2O			197.4 → 206.1	216.4 → 227.8	227.7 →237.8		258.1 →271.5	0.3
(±)**11/12** 2H_2O		180.0 →190.5		207.4 → 227.7	227.7 →247.7	256.9 →268.5	269.9 →276.7	0.5

[a]Temperature intervals and total change in enthalpy found when heating (rate of 10 K/min) previously cooled samples (cooling rate of 5 K/min).

The degree of hydration affected the DSC measurements at low temperatures (Table 2). Upon heating, seven enthalpic modifications are observed in (±)**9**·(1.01)H_2O when cooling at three different rates over the interval from 123 K to 293 K. When submitted to similar DSC experiments, equivalent modifications were observed for the structure (±)**9**·(1.40)H_2O where the first two intervals overlapped with lowering of the total enthalpy. Notably, the temperature intervals were shorter when the water content increased. The most important enthalpy variation observed in the highly pure structure (±)**9***·(1.37)H_2O with an equal content of water was that the temperature intervals were shorter and the higher temperature modifications were lost. These observations associated the observed enthalpy modifications with changes not only in the mobile appendages but also in the structural behavior of water.

The difference of the water behavior on the samples (±)**9**·(1.40)H_2O (less pure) and (±)**9***·(1.37)H_2O (highly pure) is manifested in the DSC experiments carried out at higher temperatures (Figure 9A) and in the temperature-dependent FIR studies (Figure 9B). The DSC experiments carried out on a sample of (±)**9***·(1.37)H_2O over the temperature interval 293 K→403 K gave a well-defined peak at the temperature interval 337.5 K→387.8 K (ΔH = 134.3 J·g^{-1}), which should correspond to the melting of the sample overlapped with the loss of water (Figure 9A). A second peak is observed in the interval of temperature 402.0 K→423.0 K (SI). The DSC experiment carried out on the less pure sample (±)**9**·(1.40)H_2O gave a wide curve with three peaks, which overlapped in the temperature interval 315.6 K→401.3 K (ΔH = 214.4 J·g^{-1}), where again the water loss is overlapped with the melting of the sample. In the FIR absorption spectra for (±)**9**·(1.40)H_2O and (±)**9***·(1.37)H_2O samples, the absorbance in the case of the less pure sample showed a larger temperature-dependence indicating a less compact structure (Figure 9B). Since the content in water is practically the same in both pores, enlargement of the pore diameter in (±)**9**·(1.40)H_2O, which would increase water dynamics, may be caused by the presence of the diastereomer **10** that possesses a *β*-methyl appendage.

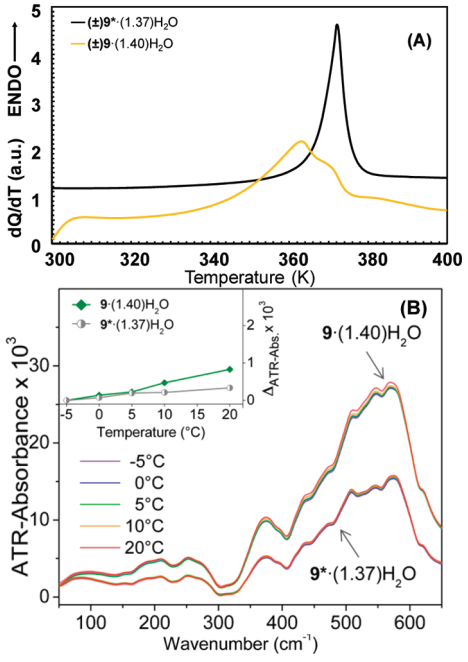

Figure 9. Measurement results of samples (±)**9**·(1.40)H_2O and (±)**9***·(1.37)H_2O with similar content of water but different purity degrees. (A) DSC results in the temperature range 300−400 K. (B) Temperature-dependent FIR spectra. Inset: Plots of the difference in integrated absorbance over the frequency range from 400 to 570 cm^{-1} at different temperatures.

Molecules **11** and **12** differ from **9** and **10** by the presence of a terminal allyl instead of a propyl appendage. An inseparable 1:1 mixture of diastereomers **11** and **12**, (±)**11/12**·2H_2O, generated a structure with a very different hydration behavior. The TGA of the crystals obtained showed a one-step water loss curve that corresponded to approximately two water molecules (SI). The low-temperature (123 K → 293 K) DSC studies revealed complex enthalpy variations related to a highly kinetic behavior since the variations depended on the previous cooling rate (Table 2).

Compared to the hydrated structure (±)**9**·*n*H_2O, the most remarkable difference occurred in the FIR spectroscopy results, specifically in the temperature-dependent spectra in the case of (±)**11/12**·2H_2O (Figure 10). Indeed, the more marked

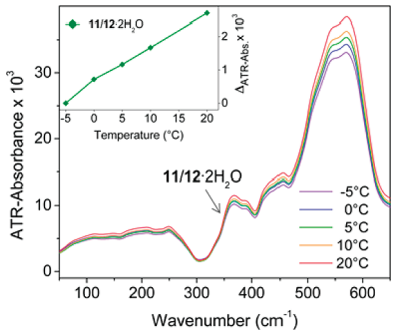

Figure 10. Changes in the pore water absorbance in the structure formed by (±)**11/12**·2H_2O from −5 to 20 °C. Inset: Plot of the difference in integrated absorbance over the frequency range from 400 to 570 cm^{-1} at different temperatures.

changes in absorbance upon increasing temperature indicate that the pore water had a higher mobility, implying a larger pore diameter. Structurally, this result can be rationalized by the pore diameter of (±)**11/12**·2H_2O being defined by a 1:1 mixture of methyl and allyl groups, whereas in the case of (±)**9**·*n*H_2O it is defined exclusively by propyl appendages. In

dx.doi.org/10.1021/jp301323c | J. Phys. Chem. C 2012, 116, 9616−9630

agreement with previous results,[47] the larger pore diameter correlated with a reduced tendency to lose water at room temperature.

(ii). Hydrated Structures Including Two/Three Carbon Appendages. We prepared structures possessing ethyl/propyl, (±)**13**·2H_2O and (±)**14**·2H_2O, and ethyl/allyl, (±)**16**·2H_2O, appendages. From the racemic molecules **13** (*β*-propyl/*α*-ethyl) and **14** (*β*-ethyl/*α*-propyl), only hydrated structures were obtained. The TG analysis of (±)**13**·2H_2O showed that the dehydration occurred in two well separated steps, the first accounting for 1.94% (309 K→ 354.1 K) of the mass, and the second for 11.39% (354.1 K→ 414.9 K). The TG analysis of (±)**14**·2H_2O showed that the water loss also proceeded in two steps in the temperature intervals 323 K→ 373 and 373 K→ 403 K. In the latter case, the mass loss is similar, corresponding to approximately 50% of the total in each case (DSC and TG results for all mentioned compounds can be found in the SI).

The racemic molecule **16** (*β*-ethyl/*α*-allyl) gave rise to both hydrated and anhydrous structures. We could not isolate any structure formed by its diastereomer (±)**15** (*β*-allyl/*α*-ethyl), but it was present in the hydrated structures formed by (±)**16**·2H_2O as a minor impurity. However, after successive crystallizations, it was possible to isolate crystals formed by pure (±)**16**, without (±)**15**, termed (±)**16***·2H_2O. The TG analysis of the hydrated samples shows a 14.19% mass loss for (±)**16**·2H_2O and a 13.82% mass loss for (±)**16***·2H_2O, both values being higher than the theoretical 12.41% calculated for two water molecules. This is most likely due to some overlapping partial evaporation of the monomer. The TG study of the hydrated structure (±)**16**·2H_2O showed that the dehydration occurred in three steps corresponding to 8.76% (304 K→336.6 K), 2.83% (336.6 K→378.0 K) and 2.61%(378.0 K→ 423.0 K) of the mass loss. The TG analysis shows that the structure (±)**16***·2H_2O is dehydrated in two steps corresponding to 9.35% (308.0 K→ 352.6 K) and 4.47% (352.6 K→ 414.3 K).

The low-temperature DSC study (123 K → 293 K) for (±)**13**·2H_2O, (±)**14**·2H_2O, (±)**16**·2H_2O, and (±)**16***·2H_2O (Table 3) showed variable behavior according to the diameter of the pore and the water content. A similar analysis of hydrated structures possessing identical appendages, (±)**8**·2H_2O (diethyl) and (±)**19**·2H_2O (diallyl), is included for comparative purposes.

The temperature intervals for structures with different appendages and narrower diameters occurred at lower temperatures and were much more complex than those structures with identical appendages. A decrease of enthalpy was observed at the lower temperature intervals among structures with identical and different appendages that can be associated with a higher molecular organization of the former structures.

For structure (±)**13**·2H_2O (*β*-propyl/*α*-ethyl), DSC experiments in the temperature interval 293.0 K → 403.0 K revealed two endothermic transitions (Figure 11A). The first transition in the temperature interval 340.3 K → 367.1 K is associated with the water loss, and the second starting at 368.0 K reflects the decomposition of the sample. The conversion study showed a 30% sample conversion and the total loss of water from 340.4 K to 354.0 K (Figure 11A).

The DSC study of (±)**14**·2H_2O in the temperature interval 293.0 K → 403.0 K exhibited a large endothermic peak from 320.7 K to 368.7 K, before the start of sample decomposition.

Table 3. Observed Endotherms by DSC[a] of Hydrated Structures (±)13·2H_2O, (±)14·2H_2O, and (±)16·2H_2O in Comparison with (±)8·2H_2O and (±)19·2H_2O

compound	interval (K)	ΔH° (J/g)	interval (K)	ΔH° (J/g)	ΔH°_{Total} (J/g)
(±)8·2H_2O	197.1 → 273.0	5.4	273.0 → 292.2	0.5	5.9
(±) **14**·2H_2O	200.2 → 224.4	1.0	246.7 → 256.2	0.2	1.2
	225.0 → 235.2		256.2 → 271.6		
	235.2 → 246.2		271.6 → 281.2		
(±) **16**·2H_2O	185.5 → 205.7	0.5	226.2 → 236.2	0.4	0.9
	208.9 → 225.7		246.1 → 272.3		
(±) **16***·2H_2O	159.8 → 175.5	1.5	221.4 → 240.5	0.5	2.0
	175.5 → 198.2		240.5 → 249.2		
	198.2 → 217.2		255.6 → 265.7		
(±) **19**·2H_2O	196.8 → 226.1	2.6	257.7 → 286.1	1.6	4.2
(±) **13**·2H_2O	187.2 → 241.2	1.1	241.2 → 264.0	0.52	1.3

[a]Temperature intervals and changes in enthalpy found when heating (rate of 10 K/min) previously cooled samples (cooling rate of 5 K/min).

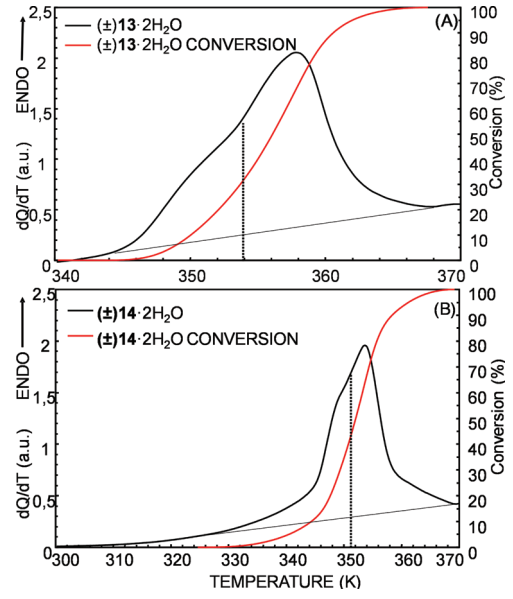

Figure 11. (A) DSC results for (±)**13**·2H_2O in the temperature interval 293 K → 403 K. The conversion study is represented by the red line. (B) DSC results for (±)**14**·2H_2O. The red curve represents the conversion study.

This peak displayed a maximum at ~348 K corresponding to the water loss. Between 321.0 and 351.2 K, 42% of sample conversion and total water loss are accomplished (Figure 11B).

The FIR spectroscopy study in the range of interest produced a different trend for (±)**14**·2H_2O compared to the diastereomer (±)**13**·2H_2O with higher variations in the absorbance as the temperature increased. This outcome is consistent with pores of larger diameter that arise from the

dx.doi.org/10.1021/jp301323c | J. Phys. Chem. C 2012, 116, 9616−9630

shorter β-oriented appendage; thus, the contained water is less restricted and exhibits higher dynamics (Figure 12).

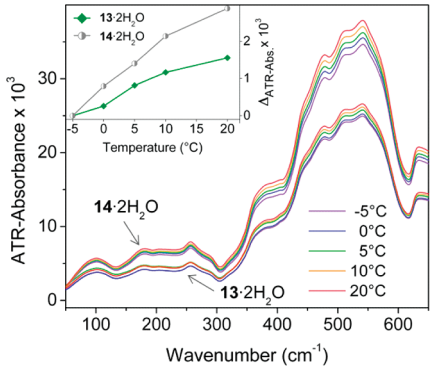

Figure 12. Temperature dependence of FIR spectra for (±)**13**·2H_2O and (±)**14**·2H_2O. Inset: Plot of the difference in integrated absorbance over the frequency range from 400 to 570 cm^{-1} at different temperatures.

The DSC study of (±)**16**·2H_2O and (±)**16***·2H_2O over the temperature interval 273 K → 423 K exhibited notable differences (Figure 13A). In the case of (±)**16**·2H_2O, a

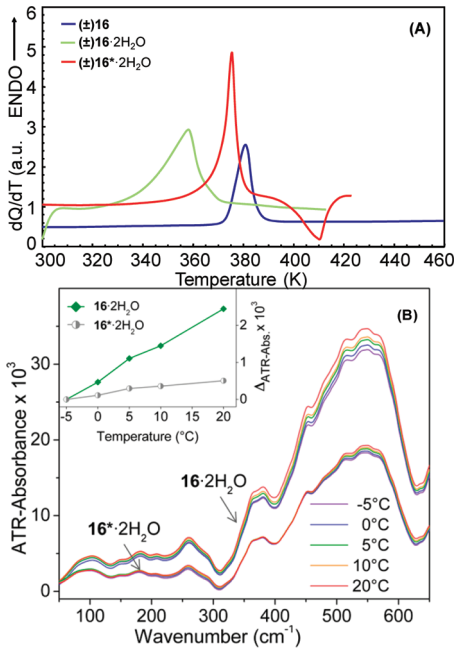

Figure 13. (A) DSC studies for the anhydrous structure (±)**16** and the hydrated (±)**16**·2H_2O (partially impure) and (±)**16***·2H_2O (highly pure) structures. (B) Study of the FIR absorbance variation with temperature for the hydrated pores (±)**16**·2H_2O and (±)**16***·2H_2O. Inset: Plot of the difference in integrated absorbance over the frequency range from 400 to 570 cm^{-1} at different temperatures for the two studied samples.

broad endothermic signal formed by three overlapping peaks was detected in the temperature interval 315.1 K → 395.2 K. On the other hand, the curve for (±)**16***·2H_2O presented a broad well-defined peak in the interval 331.5 K → 388.8 K followed by an exothermic peak that was initially assigned to a recrystallization process. This possibility, previously observed for (±)**8**·2H_2O and (±)**19**·2H_2O, was discarded for (±)**16***·2H_2O after performing VT-PXRD experiments on this sample that did not show a crystalline phase transition[47] (SI).

Interestingly, the temperature dependence of the FIR absorbance was very different for both hydrated structures, revealing the importance of the purity in the compacting of the pore (Figure 13B). The sample (±)**16**·2H_2O partially contaminated by the diastereomer (±)**15** exhibited larger variations in the absorbance upon increasing the temperature than the pure sample (±)**16***·2H_2O. This indicates higher water diffusion and consequently less restriction in the presence of crystal defects. The absence of these defects in the pure structure allows a higher degree of compacting, implying a reduction of the pore diameter.

(iii). Hydrated Structures Including Three/Three Carbon Appendages. The racemic compound **17** (β-allyl, α-propyl) tended to crystallize, giving rise to both hydrated tubular structures, (±)**17**·(1.06)H_2O, as well as anhydrous assemblies, (±)**17**. The total water loss on the hydrated sample observed by TGA (6.25%) accounted for approximately one water molecule that is released in the temperature interval 365.4 K → 413.3 K. On the other hand, all isolated samples corresponding to compound **18** (β-propyl, α-allyl) showed hydrated tubular pores with a variable degree of water content and some extent of impurity caused by the presence of its diastereomer **17**, structures (±)**18**·(1.16)H_2O and (±)**18**·(1.84)H_2O. A highly pure sample of molecule **18** was distinguished with an asterisk, (±)**18***·(1.09)H_2O. Figure 14 shows the TGA results for the

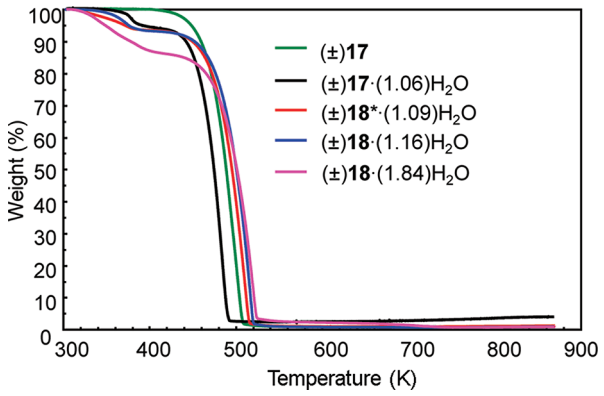

Figure 14. Comparison between the TGA results for (±)**17**, (±)**17**·(1.06)H_2O, (±)**18***·(1.09)H_2O, (±)**18**·(1.16)H_2O, and (±)**18**·(1.84)H_2O.

structures formed by compound **17**, anhydrous, (±)**17**, and hydrated, (±)**17**·nH_2O, compared to the corresponding curves for different hydrated samples of **18** [(±)**18**·nH_2O, $n \leq 2$].

The low-temperature DSC study (123 K → 293 K) (Table 4) showed variable behavior according to the hydration and diameter of the pore. On heating, seven enthalpic modifications were observed in (±)**17**·(1.06)H_2O when cooling at three different rates over the interval from 123 K to 293 K. When submitted to similar DSC experiment conditions, equivalent modifications were observed for structure (±)**18**·(1.16)H_2O where the second and third intervals are overlapped, and intervals 4−6, which occur with concomitant lowering of the total enthalpy, were not observed. When the water content increased, (±)**18**·(1.84)H_2O, the intervals 1−3 and 4−6 are overlapped. Furthermore, lower temperature intervals were shorter when the water content in the pore increased. The most important enthalpy variation was observed in the highly pure

dx.doi.org/10.1021/jp301323c | J. Phys. Chem. C 2012, 116, 9616−9630

Table 4. Observed Endotherms by DSC[a] of Hydrated Structures (±)17·(1.06)H_2O, (±)18*·(1.09)H_2O, (±)18·(1.16)H_2O, and (±)18·(1.84)H_2O

compound	interv$_1$ (K)	interv$_2$ (K)	interv$_3$ (K)	interv$_4$ (K)	interv$_5$ (K)	interv$_6$ (K)	interv$_7$ (K)	$\Delta H°$ (J/g)
(±)**17** (1.06)H_2O	175.8 →192.5	193.4 → 204.1	205.6 →217.9	218.4 →230.3	230.2 →236.8	237.1 →255.0	257.7 →276.2	0.90
(±)**18** (1.16)H_2O	190.1 →199.8		199.8 → 221.4		not observed		260.6 →281.2	0.39
(±)**18** (1.84)H_2O		186.4 → 216.7			218.2 → 259.7		259.7 →273.5	0.65
(±)**18***(1.09)H_2O	186.8 →197.4		203.5 →228.6			235.3 →249.4	265.0 →274.4	0.5

[a]Temperature intervals and total change in enthalpy found when heating (rate of 10 K/min) previously cooled samples (cooling rate of 5 K/min.

structure (±)**18***·(1.09)H_2O in comparison with (±)**18**·(1.16)H_2O. Both structures contained similar water content, and all the temperature intervals were observed, even though there was some overlap. Since the basic pore structure should remain unaltered at these temperatures, these facts, added to the reversibility of the process (supported by consecutive results with the same sample), identified enthalpy modifications with changes not only in the mobile appendages but also in the structural behavior of water itself.

The high temperature DSC experiments (range 293 K→ 413 K) were in agreement with the TGA results for (±)**17**·(1.06)H_2O. A clear endothermic peak with two superimposed maxima was observed in the temperature interval 319.9 K → 411.7 °C. This interval is coincident with the water loss temperature range. In the case of the anhydrous structure formed by (±)**17**, the clean and well-defined endothermic peak corresponds to the fusion of the sample in the interval 359.9 K→ 394.8 K (Figure 15).

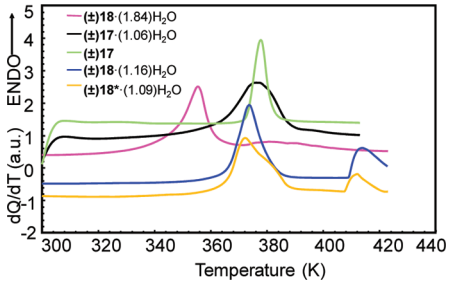

Figure 15. Comparison of the high temperature DSC results for (±)**17**, (±)**17**·(1.06)H_2O, (±)**18***·(1.09)H_2O, (±)**18**·(1.16)H_2O, and (±)**18**·(1.84)H_2O.

A comparative DSC study of structures (±)**18***·(1.09)H_2O, (±)**18**·(1.16)H_2O, and (±)**18**·(1.84)H_2O over the temperature interval 273 K → 423 K exhibited notable differences. In the case of (±)**18***·(1.09)H_2O, a broad endothermic signal formed by two overlapping peaks was detected at the temperature interval 337.0 K → 405.5 K. On the other hand, the curves for (±)**18**·(1.16)H_2O and (±)**18**·(1.84)H_2O presented broad well-defined endothermic transition peaks at the temperature intervals 346.0 K→ 395.5 and 320.7→ 372.0 K, respectively. Figure 16 illustrates the FIR absorbance spectra of hydrated structures formed by compound **17** and the hydrated structure formed by **18**. Indeed, water clusters confined in pores possessing *β*-allyl, (±)**17**·(1.06)H_2O, and *β*-propyl, (±)**18**·(1.16)H_2O, appendages, exhibited similar increases in absorbance upon increasing temperature.

In summary, the results that we have gathered concerning a small library of chemically related hydrated and anhydrous structures have contributed to our understanding of the most important features that characterize each option.

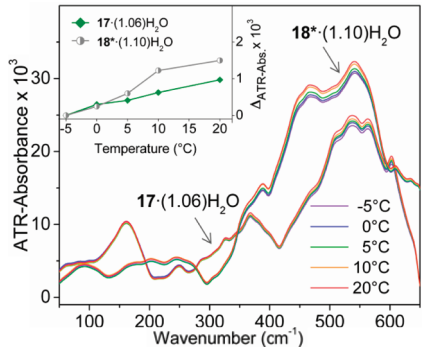

Figure 16. FIR spectroscopy study of the absorbance variation upon increasing temperature for the hydrated structures formed by (±)**17** and (±)**18**. Inset: Plot of the difference in integrated absorbance over the frequency range from 400 to 570 cm^{-1} at −5 to 20 °C.

^{13}C CP SSNMR experiments performed on (±)**19**·2H_2O allowed us to qualitatively distinguish among rigid and flexible positions in the molecule, as well as to identify the positions whose mobility was affected by temperature. The carbons of the appendages were more flexible, and this flexibility was more temperature dependent than carbons in the core of the molecule. Variable temperature T_1 experiments at different temperatures confirmed that upon decreasing temperature, the positions of the appendages become more rigid. On the other hand, the T_1 experiments before and after gas phase deuteration did not point to the participation of mobile water in the relaxation mechanism of these carbons. Relaxation appears to have an important, if not exclusive, intramolecular contribution that is mainly associated with the motion of the allyl chains. This is consistent with previous DSC results[33] as well as with the results achieved in the present work, as enthalpic changes over similar temperature intervals were found for both hydrated and anhydrous compounds. For this reason, conformational changes in the appendages are the origin of the observed results in both SSNMR and DSC experiments.

The accumulated results concerning molecules **8** − **19** (Chart 1) allowed us to reach conclusions useful for the understanding of the dynamics of confined water as a function of the structural and dynamic characteristics of the water containing pores. Our findings substantially differ from predictions of water channel diffusion theories[20−25] and may indicate that a new conceptual understanding needs to be developed.

The racemate formed by the molecule **10** always crystallizes as an anhydrous assembly, and gives insights into the strong structural conditioning conferred by the *β*-oriented appendage. For molecules **2** and **3**, the methyl appendage is of insufficient size to allow the required compacting of the cyclic structure that forms the pore. This situation is at odds with that observed for molecules **16** and **17**, which are able to simultaneously form anhydrous ((±)**16** and (±)**17**) and hydrated ((±)**16**·2H_2O

dx.doi.org/10.1021/jp301323c | J. Phys. Chem. C 2012, 116, 9616−9630

and (±)**17**·2H$_2$O) structures. This can be explained by the coexistence of both types of organization in solution at the point where the irreversible nucleation toward the crystalline state starts. Interestingly, in contrast to **10**, the assembly formed by the 1:1 mixture of diastereoisomers **11** and **12**, (±)**11**/**12**·2H$_2$O, always forms hydrated pores. The methyl appendages of **12** and the allyl appendages of **11** are arranged in the *β* oriented position, allowing the compacting of the cyclic "basic unit" of the pore.

The higher water dynamics observed by FIR studies for the structures (±)**14**·2H$_2$O and (±)**16**·2H$_2$O, similar to that observed for (±)**8**·2H$_2$O,[47] are rationalized by assuming equivalent pore diameters resulting from the presence of a *β* oriented ethyl appendage in the aforementioned cases (Figure 17, left). Similarly the water contained in the tubular structures

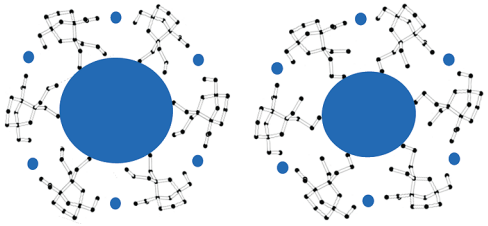

Figure 17. Graphical representation of the packing for the general structure (±)**1**·2H$_2$O (Table 1), where R2(*β*-oriented) is an ethyl appendage (structures formed by 8, 14 and 16, left side of the figure) or a propyl or allyl appendage (structures formed by **9**, **11**, **13**, **15**, **17**, **18**, **19**, right side of the figure).

formed by the racemates of molecules **9**, **11**, **13**, **15**, **17**, and **18** with propyl or allyl *β*-oriented appendages is expected to exhibit a similar dynamics to that seen in (±)**19**·2H$_2$O[47] (Figure 17, right).

With respect to the reversible or irreversible effects of temperature previously reported for "model" pores (±)**8**·2H$_2$O and (±)**19**·2H$_2$O,[44,47] the absorbance observed in the FIR spectra decreases as the water content decreases, although the changes upon varying temperature remain reversible as long as the temperature does not exceed 30 °C. This result shows that for a given pore diameter, the decrease of water content results in a decrease of mobility of the remaining water. The structure of the remaining water has changed and thus has acquired different properties. We have observed that the loss of water occurs at lower temperatures in (±)**19**·2H$_2$O that has a narrower pore diameter. These results (including the temperature intervals of interest) coincide with previous observations obtained by VT-PXRD, TGA, and DSC studies.[47]

When comparing the water dynamics in the pores formed by the molecules **9**–**18**, the results obtained for pores with equal water content must be taken into account. Especially in the case of narrow pores, a certain amount of the water can be lost even at room temperature. The plots corresponding to the dependence of FIR absorbance on temperature for different structures that form pores with the same water content are presented in Figure 18 (with the exception of **9** and **18**, which have less water content). Clearly, the dependence is much higher for the wide pore structures than for the narrow pore structures. The group formed by the structures exhibiting higher water dynamics consists of molecules that present *β*-oriented ethyl appendages, implying wider pore diameters than those of the group formed by the structures exhibiting lower water dynamics, with molecules that present *β*-oriented propyl appendages and subsequently smaller pore diameters. The pore formed by a 1:1 mixture of molecules **11** and **12** ((±)**11**/**12**·2H$_2$O) that alternates methyl and propyl appendages in the *β* orientation can be assigned to the large diameter pore group with *β*-oriented ethyl appendages. On the other hand, the plots corresponding to samples with less water content point to a decrease in the water dynamics, as is the case for (±)**8**·2H$_2$O after 45 min at 40 °C (Figure 5) or for (±)**9**·*n*H$_2$O and (±)**18***·(1.1)H$_2$O (Figure 18, middle). The purity of the samples was also very important, since frequent contamination by the corresponding diastereomer occurs. In cases where separation by crystallization is difficult, the water dynamics in the resulting pore structure increases. The less contaminated the sample, the more compact the crystal structure and the smaller the pore diameter. Contamination might imply crystal defects that result in a larger effective pore. Figure 18, right, shows examples for selected structures formed by molecules **9** and **16**. The effect is especially significant in the case of structures formed by molecule **16**, with pores that contain the "total" amount of water (two water molecules per organic monomer). The TGA and DSC results show that water loss often occurs in two steps, the first below 100 °C, and the second upon reaching 150 °C. The amount of water lost in each step depends on the pore diameter and on the water content. The dehydration temperature interval is so wide that it frequently overlaps with the fusion of the sample, so that the endotherms corresponding to each of the processes are difficult to calculate. Interestingly, the dehydration in diastereomers with equal water content but different pore diameter, occurs over a much wider temperature interval—starting at lower temperature and

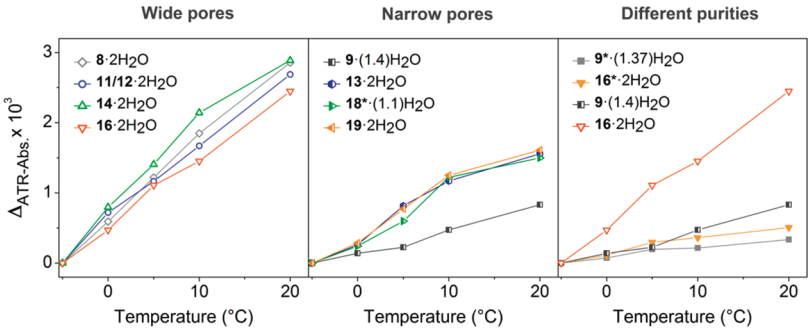

Figure 18. Comparison of the temperature dependence of the difference in integrated absorbance over the frequency range from 400 to 570 cm^{-1} for wide and narrow pores (left and middle), and for pores formed by the same diastereomer with different degree of purity.

dx.doi.org/10.1021/jp301323c | J. Phys. Chem. C 2012, 116, 9616–9630

continuing to higher temperature—in the case of the narrow diastereomer, as was the case for (±)**13**·2H_2O (narrow) and (±)**14**·2H_2O (wide). This is in complete agreement with previous observations for (±)**8**·2H_2O and (±)**19**·2H_2O.[47] The comparison of the dehydration temperature intervals for structures in which the water content is the only difference, such as (±)**18**·(1.84)H_2O and (±)**18**·(1.16)H_2O, reveals that the dehydration takes place at lower temperatures as the water content increases. For structures with the same water content but different degrees of purity, such as (±)**18***·(1.1)H_2O and (±)**18**·(1.16)H_2O, the water loss starts at lower temperature in the case of the purer sample, as the purity is correlated with the improved compacting and smaller diameter of the pore.

The water dynamics depends on the structural features that define the pores. The changes in the kinetics of the appendages that point toward the center of the pore caused by temperature variations are in agreement with the changes in the water dynamics, which represents an experimental confirmation of the thermodynamic interrelation between the contained water and the surrounding inner pore surface. The compacting of the porous structures also depends on the purity of the selected isomer. The presence of other isomers, even if only as a slight contaminant, decreases the compactness of the structure, thereby increasing the pore diameter and thus facilitating the mobility of the contained water. The diastereoisomers differ in the composition of the appendages, and it is these appendages that define the pore's interior. The low-temperature DSC studies show that the enthalpy modifications vary according to the water content in the pores, demonstrating that a thermodynamic balance exists between the water dynamics and the flexibility of the inner pore surface.

CONCLUSIONS

In the present work we have established the possibility of creating pores of general structure (±)**1**·nH_2O ($n \leq 2$) (Chart 1), by means of a thorough study of the monomers **8**−**19**. Although the crystallization mechanism to reach anhydrous (nonporous) or hydrated (porous) structures is still to be clarified, the synthesis of either type of structure is reproducible.

The water contained in these pores exhibited dynamics that could be controlled, as it depended on the structural features of the monomers that form the pore "skeleton". We have observed that the pore diameter changes depending on the selected isomer, and, at a given temperature, the arrangement and dynamics of the water contained in the pore are also different. The water dynamics increased with temperature and with the pore diameter in a process that is reversible within a certain temperature range that is specific for each structure. At temperatures higher than this particular temperature threshold, the pore water is irreversibly evacuated, and at this point, a decrease of the dynamics is observed. The elimination of the pore water starts at lower temperatures in the narrower pores, and might be observed at the moment of crystallization, even at room temperature.

These findings not only highlight the need for the presence of freely moving water inside the pore to sustain its permeability by water, but also point to the decrease in the dynamics of the residual water in the partially evacuated pores. The slower dynamics of the remaining water in partially evacuated pores is probably due to the increased interaction with the pore wall owing to the narrowing of the pore. Thus, modulation of cavity hydration by changes in the temperature and pore diameter could then enable structural determination in both open and closed pores. More importantly, this result might have biological implications as the hydrophobic gating of ion channels due to cooperative drying has been suggested as the underlying mechanism for such functions, so that the emptying of the pore is a response to, rather than the driving force for, changes in the pore width.[60,61] Our experimental observations are compatible with theoretical studies suggesting that the dynamics of water molecules that solvate hydrophobic surfaces depend on the shape of the surface.[62]

METHODS/EXPERIMENT

Solid State MAS ^{13}C NMR. For all resonance spectroscopy measurements, a Varian 600 MHz Infinity Plus spectrometer was used equipped with Spinsight Software (version 4.3.2), and a 3.2 mm HX-T3 Chemagnetics probe head. The MAS spinning rate was 10 kHz. Adamantane was used as an external reference, and the downfield peak was set to 38.48 ppm. Approximately 15 mg of compound (±)**19**·2H_2O was used for each measurement. MAS ^{13}C CP NMR: For the ^{13}C CP MAS variable contact time experiments, the Hartmann−Hahn condition[63] was set up using conventional procedures with adamantine and then accurately adjusted for the sample of interest. Contact times were varied with decreasing values from 6 to 0.1 ms. A repetition time of 4 s was chosen after appropriate ^1H T_1 measurements at each temperature (experiments were performed at 25 °C, 0 °C, −25 °C and −50 °C). 1024 accumulations were used for each different contact time. Each spectrum was deconvoluted using the Spinsight Software and build-up curves were obtained for each peak at each temperature. The experimental curves were adjusted to one of the following equations, depending of the applicable simplifications:[64]

$$I(t) = I_0(1 - T_{CH}/T_{1\rho}{}^{H})^{-1}[\exp(-t/T_{1\rho}{}^{H}) - \exp(-t/T_{CH})]$$

$$I(t) = I_0(1 - \exp(-t/T_{CH}))$$

From this fit, it is possible to obtain the T_{CH} value, which represents the efficiency of the magnetization transfer.

MAS ^{13}C T_1 Measurements. ^{13}C T_1 relaxation times were obtained with CP MAS NMR using the pulse sequence developed by Torchia.[65] The contact time was 2 ms, delay times ranged from 10 ms to 100 s, and the repetition delay was 4 s. 512 scans were accumulated for each delay time. The measurements were repeated at 25, 0, −25, and −50 °C. When using this pulse sequence, the magnetization evolution is described by the equation

$$I(t) = I_0(\exp(-(t - x_0)/T_1))$$

T_1 values for each peak of the spectra were extracted from adequate fit to this function. Spectra were deconvoluted using the Spinsight Software.

Solution NMR. ^1H, ^{13}C, COSY, HMQC, and NOESY experiments were performed in a Bruker Avance DRX-500 spectrometer (see spectra in SI). Depending on the sample, 10−20 mg of compound were dissolved in 500 μL of $CDCl_3$. The residual signal of the solvent was used as an internal parameter.

Fourier Transform Infrared-Attenuated Total Reflection (FTIR-ATR) Spectroscopy. FTIR-ATR spectroscopy[66] was used to probe the absorbance spectra of the selected

compounds and water at different temperatures. In our measurements, ATR spectra were acquired using a single-reflection ATR apparatus with a diamond internal reflection crystal (MVP-Pro of Harrick). This horizontal ATR mini-sampler with a 0.5 mm diameter sampling area was suitable for examining these sensitive substances that are easily damaged if they are pressed to form pellets for conventional transmission spectroscopic methods. The ATR unit was installed in a VERTEX 80v FTIR Spectrometer (Bruker). In our measurements, each solid sample was placed onto the surface of the ATR diamond crystal and was slightly pressed against the crystal using the built-in pressure applicator. A liquid-helium-cooled silicon bolometer detector was used for spectra acquisition in the FIR region from 50 to 670 cm^{-1}. The measurements at room temperature were carried out under light vacuum (2 mbar), and the temperature-dependent measurements were performed under nitrogen flow in the sample compartment, with temperatures ranging from −5 to 40 °C. Data collection and processing were made using OPUS software (Bruker).

TGA Experiments. Thermal stability was analyzed by TGA using a TA Instruments Q50 thermobalance with a heating rate of 10 °C/min from 30 to 600 °C in an inert (nitrogen) atmosphere with a sample purge flow of 60 mL/min.

DSC Experiments. A Mettler TA4000/DSC30 apparatus was used for the measurements. The instrument was previously calibrated in temperature and energy with reference materials.[67] The standards used for calibration were indium (T_m = 156.6 °C, ΔH_m = 28.45 KJ/kg) and zinc (T_m = 419.47 °C, ΔH_m = 108,37 KJ/kg) supplied by Mettler Toledo. In all the experiments, the samples were examined in sealed pans with perforated lids and in nitrogen atmosphere flow at a rate of 30 mL/min. All the pans with the sample were weighed on a Mettler XS105 microbalance. For the experiments at lower temperatures, the sample was equilibrated inside the calorimeter at T = 298 K and then cooled at a rate of 5 K/min until T = 150 K. The cooled sample was afterward subjected to a heating run at a rate of 10 K/min to 298 K. Then, the same sample was subjected to a cooling rate of 10 K/min followed by a heating at 10 K/min, and a new cooling at rate of 20 K/min followed by a heating rate of 10 K/min.

Purification and Isolation of Diastereoisomers ***9*****−****18****.* The compounds were purified by successive chromatography columns, fractional crystallization and/or manual separation in the cases in which the habit of the crystals allowed it. A "hydrated" or "anhydrous" sample was defined as that in which more than 98% of the crystals are found to be "hydrated" or "anhydrous". The hydrated structures were confirmed by the formation of macroscopic hollow tubular crystals after recrystallization in a closed water vapor atmosphere.[36] The identification and assessment of purity of the diastereomers was further studied by solution NMR (^1H, ^{13}C, COSY, HMQC and NOESY) experiments.

■ ASSOCIATED CONTENT

Ⓢ Supporting Information

General experimental procedures, analytical data of all compounds, NMR spectra, low-temperature DSC tables, and graphs with individual TGA, DSC, and FIR spectroscopy results. This material is available free of charge via the Internet at http://pubs.acs.org.

■ AUTHOR INFORMATION

Corresponding Author

*E-mail: jdmartin@iiq.csic.es.

Notes

The authors declare no competing financial interest.

■ ACKNOWLEDGMENTS

The financial support from the Spanish Ministry of Science and Technology (MST/FEDER, Project CTQ2007-61024/BQU) is gratefully acknowledged. This paper is dedicated to Prof. José Barluenga on the occasion of his 70th birthday.

■ REFERENCES

(1) Finkelstein, A. *Water Movement through Lipid Bilayers, Pores, and Plasma Membranes: Theory and Reality*; Wiley: New York, 1987.
(2) Agre, P. *Angew. Chem., Int. Ed.* **2004**, *43*, 4278−4290.
(3) Sui, H.; Han, B. G.; Lee, J. K.; Walian, P.; Jap, B. K. *Nature* **2001**, *414*, 872−878.
(4) Preston, G. M.; Carrol, T. P.; Guggino, W. B.; Agre, P. *Science* **1992**, *256*, 385−387.
(5) Preston, G. M.; Mitsuoka, K.; Hirai, T.; Walz, T.; Agre, P.; Heymann, J. B.; Engel, A.; Fijuyoshi, Y. *Nature* **2000**, *407*, 599−605.
(6) Ren, G.; Reddy, V. S.; Cheng, A.; Melnyk, P.; Mitra, A. K. *Proc. Natl. Acad. Sci. U.S.A.* **2001**, *98*, 1398−1403.
(7) De Grooth, B. L.; Grubmüller, H. *Science* **2001**, *294*, 2353−2357.
(8) Hummer, G.; Rasaiah, J. C.; Noworyta, J. P. *Nature* **2001**, *414*, 188−190.
(9) Andreev, S.; Reichman, D.; Hummer, G. *J. Chem. Phys.* **2005**, *123*, 194502 /1−9.
(10) Cicero, G.; Grossman, J. C.; Schwegler, E.; Gygi, F.; Galli, G. *J. Am. Chem. Soc.* **2008**, *130*, 1871−1878.
(11) ÓConnell, M. J. *Carbon Nanotubes: Properties and Applications*; CRC Press: Boca Raton, FL, 2006.
(12) Sui, H.; Han, B. G.; Lee, J. K.; Walian, P.; Jap, B. K. *Nature* **2001**, *414*, 872−878.
(13) Rasaiah, J. C.; Garde, S.; Hummer, G. *Annu. Rev. Phys. Chem.* **2008**, *59*, 713−740.
(14) Zhu, F.; Schulten, K. *Biophys. J.* **2003**, *85*, 236−244.
(15) Fang, H.; Wan, R.; Gong, X.; Lu, H.; Li, S. *J. Phys. D: Appl. Phys.* **2008**, *41*, 103002/1−16.
(16) Kolesnikov, A. I.; Zanotti, J. M.; Loong, C. K.; Thiyagarajan, P.; Moravsky, A. P.; Loutfy, R. O.; Bunham, C. J. *Phys. Rev. Lett.* **2004**, *93*, 035503/1−4.
(17) Chou, C. C.; Hsiao, H. Y.; Hong, Q. S.; Chen, C. H.; Peng, Y. W.; Chen, H. W.; Yang, P. C. *Nano Lett.* **2008**, *8*, 437−445.
(18) Tajkhorshid, E.; Nollert, P.; Jensen, M. Ø.; Miercke, L. J. W.; ÓConnell, J.; Stroud, R. M.; Shulten, K. *Science* **2002**, *296*, 525−530.
(19) Bianco, A.; Kostarelos, K.; Prato, M. *Curr. Opin. Chem. Biol.* **2005**, *9*, 674−679.
(20) Alexiadis, A.; Kassinos, S. *Chem. Rev.* **2008**, *108*, 5014−5034.
(21) Köfinger, J.; Hummer, G.; Dellago, C. *Proc. Natl. Acad. Sci. U.S.A.* **2008**, *105*, 13218−13222.
(22) Waghe, A.; Rasaiah, J. C.; Hummer, G. *J. Chem. Phys.* **2002**, *117*, 10789−10795.
(23) Won, C. Y.; Aluru, N. R. *J. Am. Chem. Soc.* **2007**, *129*, 2748−2749.
(24) Nanok, T.; Artrith, N.; Pantu, P.; Bopp, P. A.; Limtrakul, J. *J. Phys. Chem. A* **2009**, *113*, 2103−2108.
(25) Mashl, R. J.; Joseph, S.; Aluru, N. R.; Jakobsson, E. *Nano Lett.* **2003**, *3*, 589−592.
(26) Liu, Y.; Wang, Q.; Wu, T.; Zhang, L. *J. Chem. Phys.* **2005**, *123*, 234701−234707.
(27) Koga, K.; Tanaka, H.; Zeng, X. C. *Nature* **2000**, *408*, 564−567.
(28) Liu, Y.; Wang, Q. *Phys. Rev. B* **2005**, *72*, 085420/1−4.
(29) Liu, Y.; Wang, Q.; Zang, L.; Wu, T. *Langmuir* **2005**, *21*, 12025−12030.
(30) Joseph, S.; Aluru, N. R. *Nano Lett.* **2008**, *8*, 452−458.

(31) Won, C. Y.; Aluru, N. R. *J. Phys. Chem. C* **2008**, *112*, 1812−1818.
(32) Hoffmann, R.; Schleyer, Pv. R.; Schaefer, H. F., III. *Angew. Chem., Int. Ed.* **2008**, *47*, 7164−7167.
(33) Febles, M.; Pérez-Hernández, N.; Pérez, C.; Rodríguez, M. L.; Foces- Foces, C.; Roux, M. V.; Morales, E. Q.; Buntkowsky, G.; Limbach, H.-H.; Martín, J. D. *J. Am. Chem. Soc.* **2006**, *218*, 10008−10009.
(34) Barnes, C. P.; Silk, D.; Sheng, X.; Stumpf, M. P. H *Proc. Natl. Acad. Sci. U.S.A.* **2011**, *108*, 15190−15195.
(35) Yeh, B. J.; Lim, W. A. *Nat. Chem. Biol.* **2007**, *3*, 521−525.
(36) Pérez-Hernández, N.; Fort, D.; Pérez, C.; Martín, J. D. *Cryst. Growth Des.* **2011**, *11*, 1054−1061.
(37) Ashby, W. R. Principles of the self-organizing system. In *Principles of Self-Organization*; Von Foerster, H., Zopf, G. W., Eds.; Pergamon: London, 1962; pp 255−278.
(38) Eiter, T.; Gottlob, G. *Journal of the ACM* **1995**, *42.1*, 3−42.
(39) Pérez-Hernández, N.; Febles, M.; Pérez, C.; Pérez, R.; Rodríguez, M. L.; Foces-Foces, C.; Martín, J. D. *J. Org. Chem.* **2006**, *71*, 1139−1151.
(40) Ruiz-Pérez, C.; Rodríguez, M. L.; Martín, J. D.; Pérez, C.; Morales, P.; Ravelo, J. L. *Acta Crystallogr.* **1990**, *C46*, 1507−1509.
(41) Carrasco, H.; Foces-Foces, C.; Pérez, C.; Rodríguez, M. L.; Martín, J. D. *J. Am. Chem. Soc.* **2001**, *123*, 11970−11981.
(42) Pérez, C.; Espínola, C. G.; Foces-Foces, C.; Núñez-Coello, P.; Carrasco, H.; Martín, J. D. *Org. Lett.* **2000**, *2*, 1185−1188.
(43) Foces-Foces, C.; Rodríguez, M. L. Pérez, C.; Febles, M. To be published.
(44) Pérez- Hernández, N.; Luong, T. Q.; Pérez, C.; Martín, J. D.; Havenith, M. *Phys. Chem. Chem. Phys.* **2010**, *12*, 6928−6932.
(45) Foces-Foces, C.; Rodríguez, M. L.; Febles, M.; Pérez, C.; Martín, J. D. *Acta Crystallogr.* **2005**, *C61*, 339−342.
(46) Rodríguez, M. L.; Febles, M.; Pérez, C.; Pérez-Hernández, N.; Martín, J. D.; Foces-Foces, C. *Acta Crystallogr.* **2005**, *C61*, 138−142.
(47) Pérez-Hernández, N.; Falcao, E. H. L.; Pérez, C.; Fort, D.; Martín, J. D.; Eckert, J. *J. Phys. Chem. B* **2010**, *114*, 5694−5699.
(48) Pérez-Hernández, N.; Febles, M.; Pérez, C.; Spandl, J.; Martín, J. D.; Limbach, H.-H. *J. Phys. Chem. C* **2011**, *115*, 9393−9402.
(49) Yu, B.; Blaber, M.; Gronenborn, A. M.; Clore, G. M.; Caspar, D. L. *Proc. Natl. Acad. Sci. U.S.A.* **1999**, *96*, 103−108.
(50) Ernst, J. A.; Clubb, R. T.; Zhou, H.-X.; Gronenborn, A. M.; Clore, G. M. *Science* **1995**, *267*, 1813−1816.
(51) Denisov, V. P.; Venu, K.; Peters, J.; Hörlein, H. D.; Halle, B. *J. Phys. Chem. B* **1997**, *101*, 9380−9389.
(52) Clarke, H. D.; Arora, K. K.; Bass, H.; Kavuru, P.; Ong, T. T.; Pujari, T.; Wojtas, L.; Zaworotko, M. J. *Cryst. Growth Des.* **2010**, *10*, 2152−2167.
(53) Kolodziejski, W.; Klinowski. *J. Chem. Rev.* **2002**, *102*, 613−628.
(54) Natasohn, A.; Feldman, D. *J. Appl. Polym. Sci.* **1990**, *40*, 899−904.
(55) Aluas, M.; Filip, C. *Solid State Nucl. Magn. Reson.* **2005**, *27*, 165−173.
(56) Zhao, H.; Lin, W.; Yang, G.; Chen, Q. *Eur. Polym. J.* **2005**, *41*, 2354−2359.
(57) Aso, Y.; Yoshioka, S.; Zhang, J.; Zografi, G. *Chem. Pharm. Bull.* **2002**, *50*, 822−826.
(58) Kakuta, Y.; Hojo, H.; Aimoto, S.; Tanaka, I.; Hikichi, K. *J. Biochem.* **1994**, *116*, 1153−1555.
(59) Waters, J. F.; Likavec, W. R.; Ritchey, W. M. *J. Appl. Polym. Sci.* **1994**, *53*, 59−70.
(60) Jensen, M. Ø.; Borhani, D. W.; Lindorff-Larsen, K.; Maragakis, P.; Jogini, V.; Eatwood, M. P.; Dror, R. O.; Shaw, D. E. *Proc. Natl. Acad. Sci. U.S.A.* **2010**, *107*, 5833−5838.
(61) Zhu, F.; Hummer, G. *Proc. Natl. Acad. Sci. U.S.A.* **2010**, *107*, 19814−19819.
(62) Yin, H.; Hummer, G.; Rasaiah, J. C. *J. Am. Chem. Soc.* **2007**, *129*, 7369−7377.
(63) Hartmann, S. R.; Hahn, E. L. *Phys. Rev.* **1962**, *128*, 2042−2053.
(64) Levitt, M. H. Spin Dynamics. *Basics of Nuclear Magnetic Resonance*; John Wiley & Sons, Ltd.: West Sussex, England, 2006; pp 524−537.
(65) Torchia, D. A. *J. Magn. Reson.* **1978**, *30*, 613−616.
(66) Harrick, N. J. *Internal Reflection Spectroscopy*; Wiley: New York, 1967.
(67) Gmelin, E.; Sarge, S. M. *Thermochim. Acta* **2000**, *347*, 9−13.